Corrosion Science 53 (2011) 1018–1024

Contents lists available at ScienceDirect

Corrosion Science

journal homepage: www.elsevier.com/locate/corsci

Electrochemical impedance studies of the initial-stage corrosion of 310S stainless steel beneath thin film of molten $(0.62Li, 0.38K)_2CO_3$ at 650 °C

C.S. Ni, L.Y. Lu, C.L. Zeng, Y. Niu *

State Key Laboratory for Corrosion and Protection, Institute of Metal Research, Chinese Academy of Sciences, Shenyang, People's Republic of China

ARTICLE INFO

Article history:
Received 21 July 2010
Accepted 29 November 2010
Available online 15 December 2010

Keywords:
A. Stainless steel
A. Molten salts
B. EIS
C. Hot corrosion

ABSTRACT

Electrochemical impedance spectroscopy (EIS) has been used to study the initial-stage corrosion of 310S stainless steel beneath thin film of molten $(0.62Li, 0.38\ K)_2CO_3$ at 650 °C in air. Two-electrode system is used to fabricate molten-salt film. The thickness of molten salt approximated from electrolyte resistance decreases rapidly until it is smaller than 6 mg/cm^2. The appearance of diffusion-related impedance at the end of the test is linked to the severe loss of molten salt which causes twisted diffusion paths. More molten salt on the surface of 310S causes a longer lithiation process and more profound degradation of the oxide film.

1. Introduction

The high operating temperature of Molten Carbonate Fuel Cell (MCFC) enables a sufficient conductivity of the carbonate electrolyte, but it places severe demands on the corrosion stability and life span of cell components concerning the corrosivity and volatility of molten carbonate at 650 °C. On the cathode end, the separators expose to highly oxidizing environment, and, after reaction with the thin, creeping electrolyte resulted from evaporation, they form a multi-layered corrosion scale [1,2]. The hot corrosion of separator poses a significant performance-limiting issue for MCFC.

The thermogravity analysis (TGA) was usually used to study the corrosion of pure metal or alloys induced by thin films of molten carbonate [1,3–7]. Zhu et al. [1] reported the corrosion of Fe and Fe–Cr alloy under film of fused $(0.62Li, 0.38\ K)_2CO_3$ at 650 °C for 24 h and found that a double-layer scale was formed and the outer layer had large pores while the inner layer was compact with small pores. The corrosion of iron with 2 mg/cm^2 $(0.62Li, 0.38\ K)_2CO_3$ eutectic at 650 °C was controlled by the diffusion of cation through FeO and Fe_3O_4 layer under gas containing 20% O_2 [3]. Mitsushima et al. [4] proposed a model based on TGA curves to explain the accelerated corrosion of iron under $(0.52Li, 0.48Na)_2CO_3$ coating and attributed the initial-stage accelerated corrosion to the lithiation reaction between the thus formed oxide and molten carbonate. The corrosion rate of Ni under thin film of molten carbonate at 650 °C varied considerably with the thickness of salt film and the composition of gases [5,6]. Ota et al. [7] examined the corrosion of SUS310S and SUS316L in the presence of Li/K or Li/Na carbonate in the temperature range of 500–900 °C and found an accelerated corrosion at the very beginning of 60-h tests at the temperature below 650 °C.

Hot corrosion occurs through the electrochemical mechanism and more information can be gained through electrochemical tests. Electrochemical impedance spectroscopy (EIS) is a technique that has proved effective in investigating the reaction mechanisms and kinetics in hot corrosion induced by molten carbonates [8–17]. The impedance response of pure Ni, FeAl (Fe–24.4Al–0.12B wt.%), CuAl (Cu–15Al wt.%), NiTi (Ni–10, 15Ti wt.%), NiCo (Ni–50Co wt.%) and AISI 310 stainless steel (Fe–25Cr–20Ni wt.%) after different immersion time in molten carbonates at 650 °C was monitored and corresponding models were proposed to specify the corrosion mechanism [8–12]. Electrochemical impedance was also used to assess the corrosion resistance of different Cr-content alloys against molten carbonates after a given immersion period [13,14]. Frangini [15] compared the corrosion kinetics of 310S stainless steel in molten carbonates obtained with impedance spectra and linear polarization and concluded that the presence of diffusion impedance terms and formation of surface resistive films coupled with lithiation process might result in unreliable resistance values obtained with the linear polarization. Zhu et al. [16] found that the corrosion rates estimated from the two electrochemical techniques concurred only at the initial period of immersion.

However, direct electrochemical test of the corrosion induced by thin films of molten carbonates is lacking as electrochemical impedance investigations of hot corrosion induced by thin films of molten salt were confined mainly to fused sulfates and/or chlorides [18–22]. Wu and Rapp [18] employed EIS to identify three types of corrosion (passive, pseudo-passive and active) of

* Corresponding author. Tel.: +86 24 23971375; fax: +86 24 23971687.
E-mail address: yniu@imr.ac.cn (Y. Niu).

0010-938X/$ - see front matter © 2010 Elsevier Ltd. All rights reserved.
doi:10.1016/j.corsci.2010.11.036

preoxidised nickel induced by thin-fused sulfate film at 963 °C owing to different preoxidation conditions. Unlike the corrosion process of M38G in bulk melt, the corrosion induced by thin film of fused (0.9Na, 0.1 K)$_2SO_4$ showed no diffusion reaction from the initial-stage impedance spectra [21].

In this paper a two-electrode system was used to fabricate thin film of molten (0.62Li, 0.38 K)$_2CO_3$ and the EIS tests were carried out at 650 °C in air to investigate the anomalous corrosion behaviour of 310S stainless steel during the initial stage. The loss of molten salt and the lithiation process were for the first time emphasised throughout the analysis.

2. Experimental

The mixed powder of 62% Li_2CO_3 + 38% K_2CO_3 (mole fraction) had been baked in an aluminium crucible at 300 °C for 24 h to purge the trace amount of moisture before it was melted and stabilized at 650 °C. A two-electrode system was used for electrochemical impedance measurements and the electrode material was commercial 310S stainless steel whose composition was listed in Table 1. The two electrodes, sealed in high-temperature cement, separated from one another by 0.2 mm with rigorous parallelism. A distance of 0.2 mm was chosen to reduce electrolyte resistance between the gap while prevent the interaction of corrosion products on the two electrodes. The detrimental effect of the formation of oxide bridge between the two electrodes on EIS measurement was explained by Farrell et al. [20]. The rigorous positioning of the two electrodes was achieved using the method shown in the flowsheet of Fig. 1. First, line cutting was used to cut a piece of sample into the shape 100 mm × 12.2 mm × 8 mm and then to slice a 90 mm slot middle of the sample, as shown in Fig. 1a. Had being cleaned with acetone and distilled water, the sample was sealed in an alumina tube with its slot being filled with high-temperature cement. Seven days were needed for the high-temperature cement to solidify and then the alumina tube containing the sample was cut into cylinder of 8 mm long as shown in Fig. 1c. Fe–25 wt.% Cr lead wire was spot-welded to each of the electrodes to form the electrode head in Fig. 1d, which was then sealed in another wider alumina tube. Fig. 1e shows the final electrode, and then it was dried at room temperature for seven days and then grounded to 600 sand paper. The wire of line cutting was 0.18 mm in diameter, so the slot between the two electrodes was fixated to be 0.2 mm and, more importantly, remained constant for every electrode. The detailed experimental setup and dimensions of the electrode system are shown in Fig. 2 and the test

Table 1
The composition of commercial 310S in weight percent (wt.%).

Fe	Cr	Ni	Mn	P	C	S
Bal.	26.37	18.50	1.40	⩽0.045	⩽0.08	⩽0.03

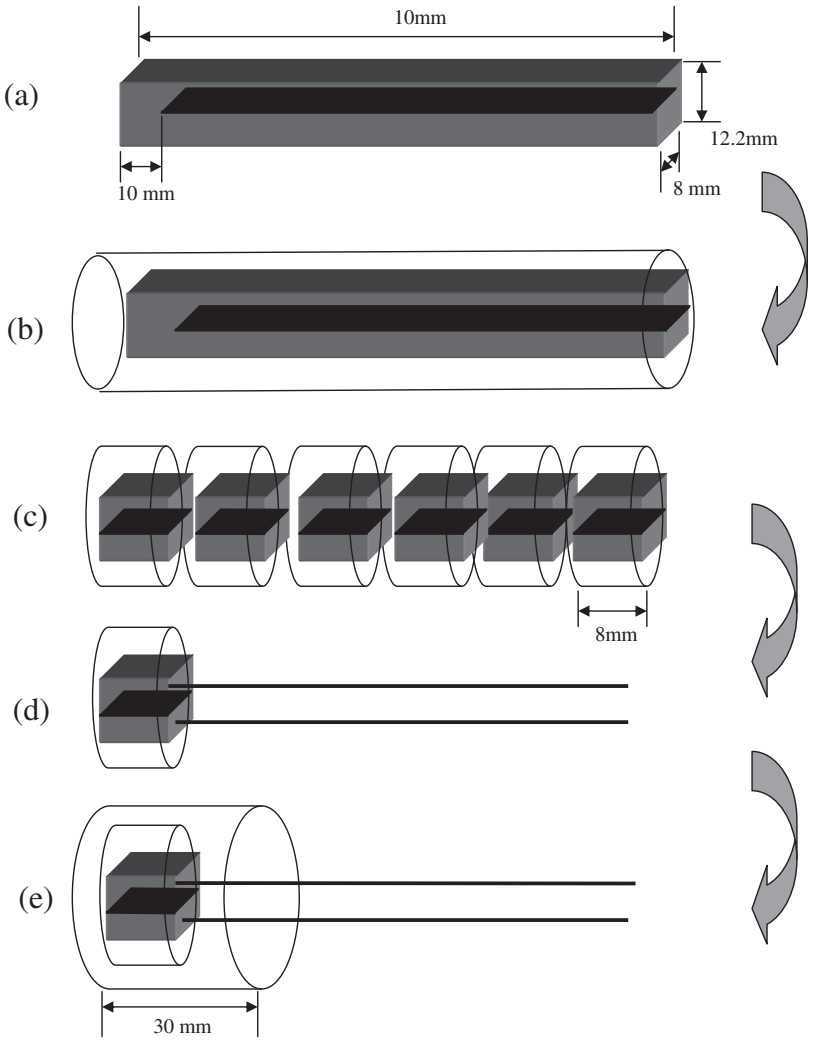

Fig. 1. Flowsheet of fabricating the electrode for the purpose of controlling the rigorous distance of 0.2 mm between the two metallic samples.

procedures were described in Ref. [21]. The electrode was dipped into the molten salt and then lifted above the molten salt surface to fabricate a thin film of molten salt on the electrode. The two metallic samples were connected by the thin film of molten salt on the high-temperature cement between them. Two runs of experiment using fresh electrodes, defined as test one and test two, were conducted to study the influence due to the variance of the thickness of molten salt on the corrosion process.

The electrochemical impedance measurements were carried out in the frequency range of 10^5 Hz–10^{-2} Hz using a computer-controlling high-speed Parstat 2273 of Princeton Applied Research. The amplitude of input sine signal was 10 mV. The impedance spectra were calculated and fitted using Zview software.

At the end of the test, the electrode had been taken out of the furnace and cooled down at room temperature before it was characterised by a scanning electron microscopy (SEM) equipped with energy dispersive X-ray microanalysis (EDX).

3. Results and discussion

3.1. Calculated thickness of molten salt on the electrode

The electrolyte resistance, R_e, was caused between the two separate electrodes by the highly conductive molten salt which was a cuboid on the 0.2 mm gap X_G with a length of 6 mm X_L and a height of the thickness of electrolyte δ_T. Therefore, the δ_T can be achieved by

$$\delta_T = X_G/(X_L R_e \sigma) \quad (1)$$

where σ is the electric conductivity of the molten salt at 650 °C. The weight of molten salt on unit area, δ_W, can be calculated by

$$\delta_W = \rho X_G/(X_L R_e \sigma) \quad (2)$$

where ρ is the density of the molten salt at 650 °C.

Fig. 3 shows the high-frequency Nyquist plot at the very beginning of molten-salt corrosion (one minute after the fabrication of salt film) of test one. The resistance of the cuboid on the 0.2 mm gap, i.e. the unnormalised value R_e between the two electrodes, can be approximated by the intersection between the Nyquist plot and the Zr scale, indicating an unnormalised R_e of 6.95 Ω for test one at one minute. The values of σ and ρ are reported to be 0.39 Ω^{-1} cm^{-1} and 1.91 g/cm^3 [23,24], respectively. Therefore, the thickness of electrolyte by weight, δ_W, at different time for test one and two can be calculated in the same way and plotted vs. time, as is shown in Fig. 4. The left and right ordinate represents $1/R_e$ and δ_W, respectively. Fig. 4 shows that the initial δ_W of test two is higher than that of test one by 4 mg/cm^2 (23.4 mg/cm^2 for test one compared with 27.5 mg/cm^2 for test two) and both decrease drastically until δ_W approaches 6 mg/cm^2 and level off onward. The loss of molten salt can be attributed to the evaporation of molten salt at 650 °C since this temperature is much higher than the melting point of the mixed salt, 486 °C.

3.2. The variation of polarization resistance R_p with time

The polarization resistance R_p was obtained by subtracting the high frequency impedance at 10 kHz from the low frequency impedance at 10 mHz. The corrosion rate is proportional to the reciprocal of polarization resistance using the Stern–Geary equation [20,25]

$$\text{Corrosion rate} = K/R_p \quad (3)$$

$$K = b_a b_c/(2.303(b_a + b_c)) \quad (4)$$

where b_a and b_c is anodic and cathodic Tafel slopes, respectively. The value of K is a function of metal and electrolyte and can be assumed to be constant for a given metal-electrolyte system. The data of $1/R_p$ vs. exposure time are shown in Fig. 5. The values of $1/R_p$ of

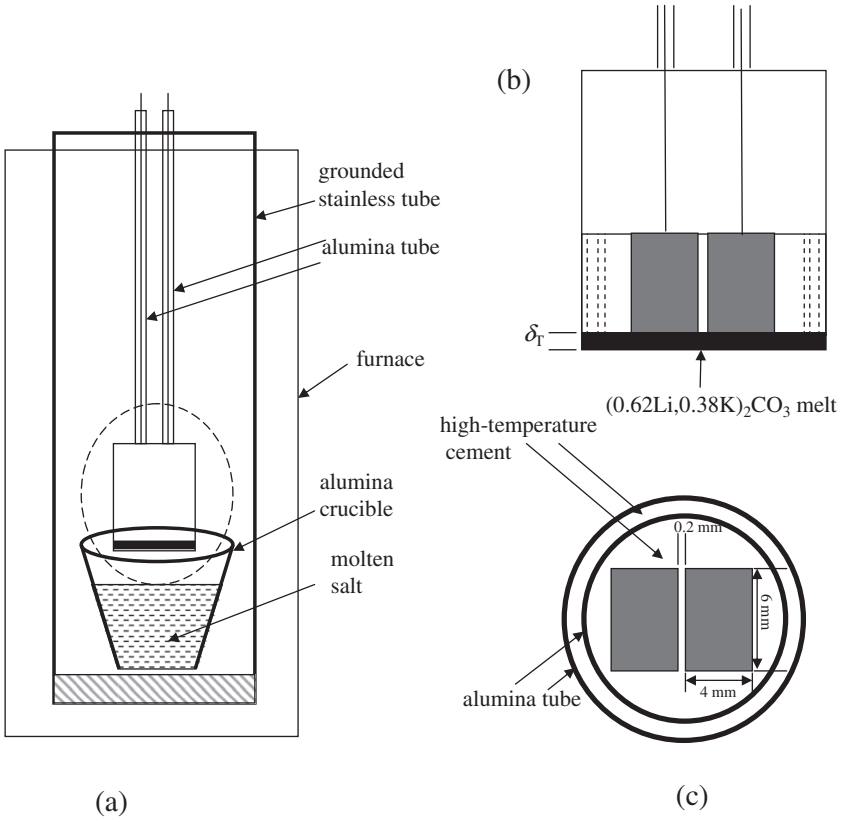

Fig. 2. Schematic of the experimental setup and the dimensions of the electrode; (b) is the enlarged view of the oval area in (a and c) the top view of the electrode.

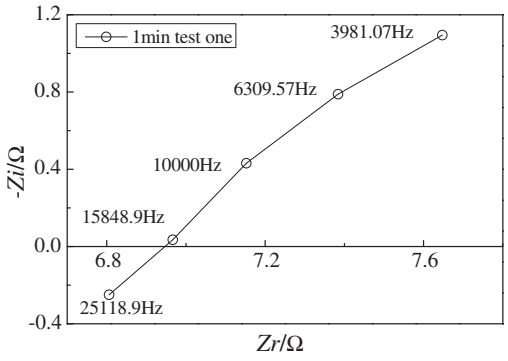

Fig. 3. High-frequency Nyquist plot before being normalized by area at the exposure time of 1 min of test one.

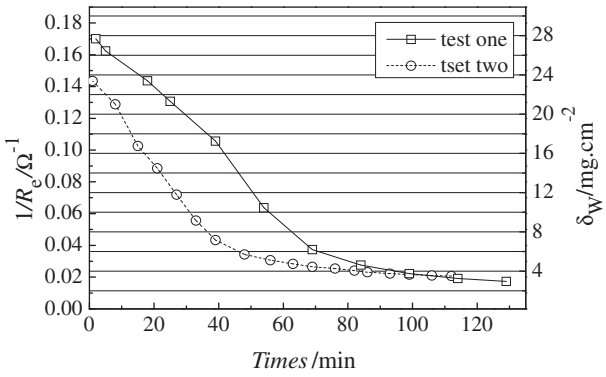

Fig. 4. Plots of $1/R_e$ and calculated δ_w vs. exposure time of test one and test two.

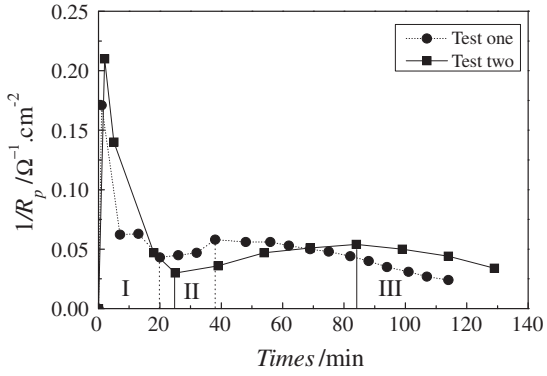

Fig. 5. Monitoring results of $1/R_p$ vs. the exposure time of test one (dashed lines) and test two (solid lines).

test one and two decrease rapidly to a minimum corresponding to 20 min and 25 min, respectively, and then rise to a maximum at 38 min and 84 min, respectively, before they decrease once again. Therefore, the corrosion process can be divided into three stages: the corrosion rate begins at a high value and then decrease to the minimum at the end of stage I; the corrosion rate starts to rise until the end of stage II; from the end of stage II onward, the corrosion rate decreases again and this is stage III. Fig. 5 shows evidently a longer duration of stage II with a thicker salt film.

3.3. Impedance spectra of stage II and III

3.3.1. Impedance spectra of stage II

The impedance spectra of test one at 20 min and 32 min are superimposed in Fig. 6 and those of test two at 25 min, 39 min,

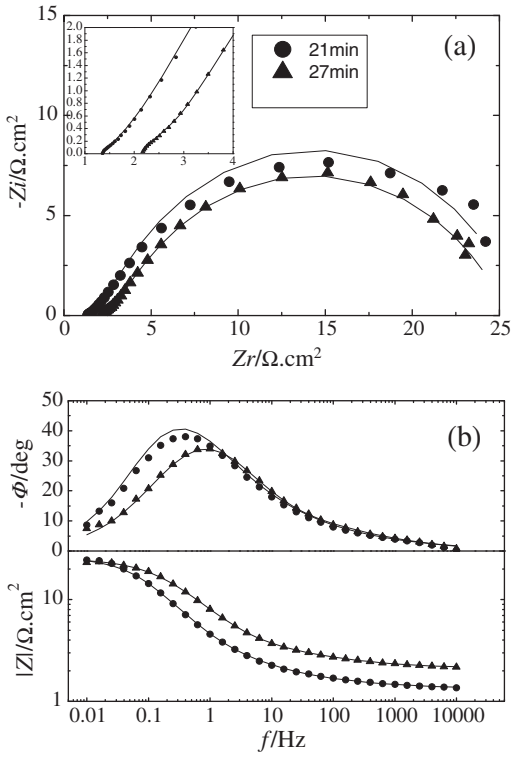

Fig. 6. Nyquist and Bode plots for the corrosion induced by thin film of molten carbonate during the stage II of test one at 650 °C in air: (a) Nyquist plots and (b) Bode plots. Symbol: experimental data and line: simulation data.

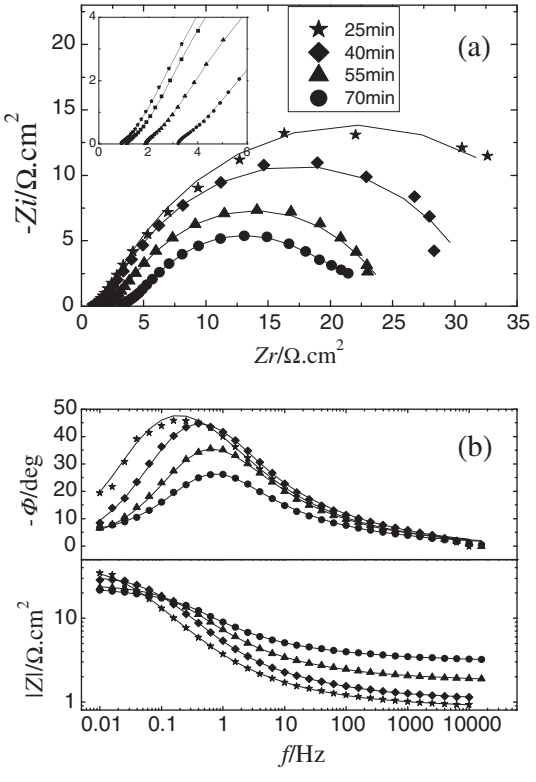

Fig. 7. Nyquist and Bode plots for the corrosion induced by thin film of molten carbonate during the stage II of test two at 650 °C in air: (a) Nyquist plots and (b) Bode plots. Symbol: experimental data and line: simulated data.

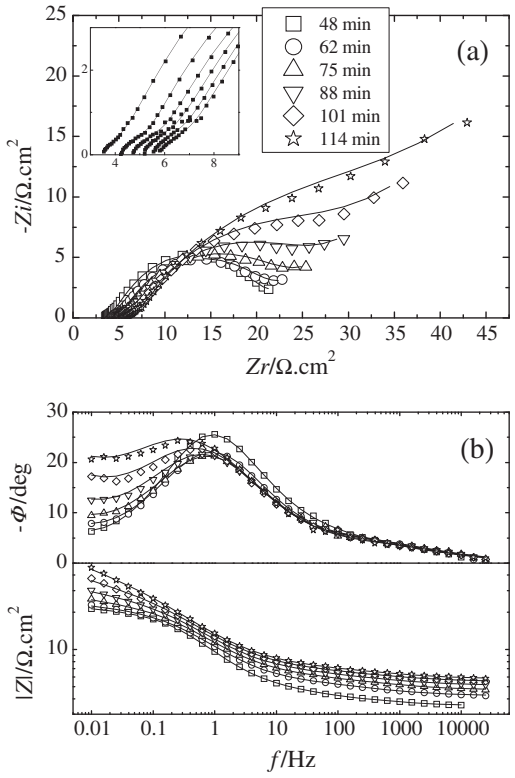

Fig. 8. Nyquist and Bode plots for the corrosion induced by thin film of molten carbonate during the stage III of test one at 650 °C in air: (a) Nyquist plots and (b) Bode plots. Symbol: experimental data and line: simulated data.

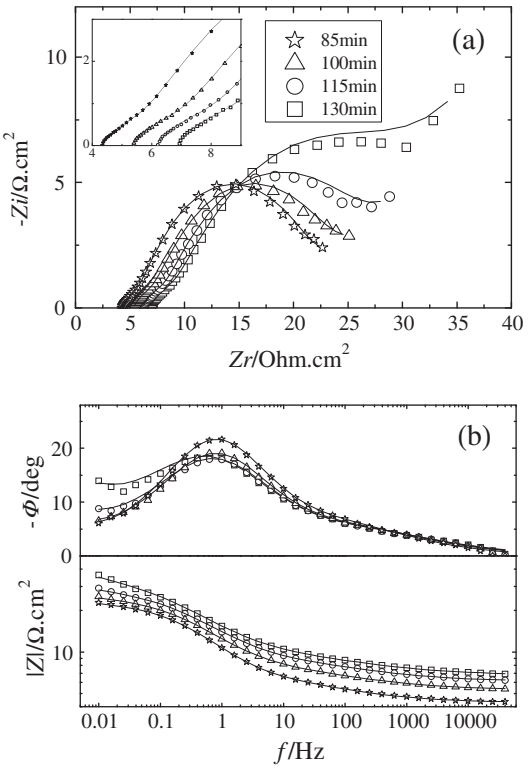

Fig. 9. Nyquist and Bode plots for the corrosion induced by thin film of molten carbonate during the stage III of test two at 650 °C in air: (a) Nyquist plots and (b) Bode plots. Symbol: experimental data and line: simulated data.

54 min and 69 min in Fig. 7. The spectra consist of two depressed loops, a very small one at high frequency (as illustrated in the inserts) and a large one at low frequency. Judging from the plots of phase angle ($-\Phi$ vs. $log(f)$, the time constant at high-frequency port cannot be distinguished well. Under thin carbonate, the transport of oxygen is insignificant after fast corrosion in stage I since no diffusion-related impedance is found.

3.3.2. Impedance spectra of stage III

Fig. 8 and Fig. 9 are the impedance spectra of test one and two at different exposure time during stage III. The major difference of impedance at this stage from stage II is the appearance of diffusion tail at the low frequency, which becomes more salient as the time of exposure progress. The Bode plots show that the modulus of impedance $|Z|$ at all frequencies increases with time.

Examination of the corroded samples of test one indicates that a porous scale is formed on the surface and no Cr-rich layer is detected, as is shown in Fig. 10. The bright particles on the outer scale are slightly rich in Ni and the distribution of metallic elements (Fe, Cr and Ni) is similar to the alloy substrate elsewhere. EDX also indicates the existence of potassium in the scale. The surface morphology of the corroded sample (Fig. 11) shows a rough and loose surface of oxide crystals which are interspersed by

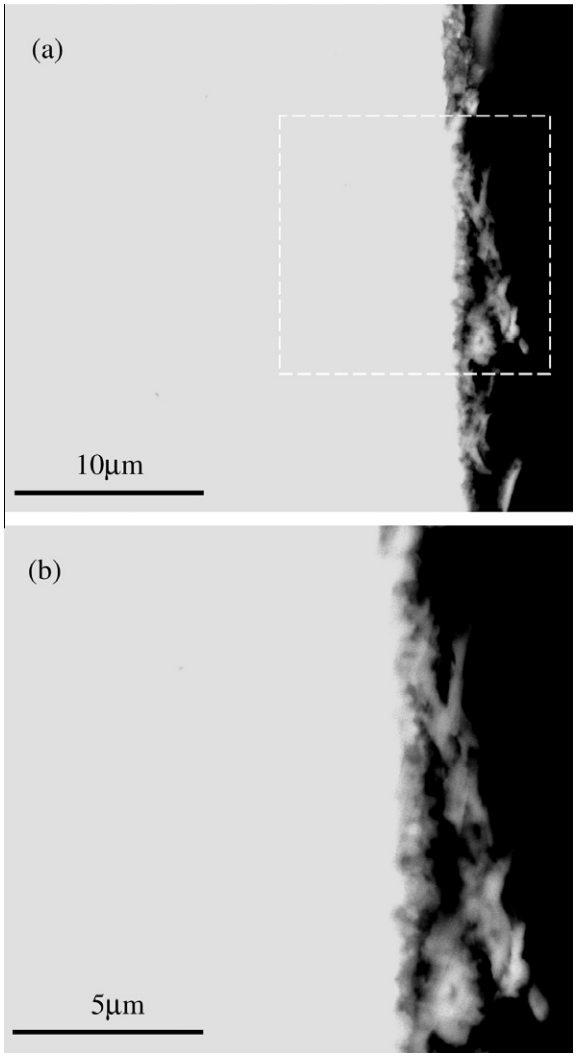

Fig. 10. Cross-sectional morphologies of 310S of test one after 120 min corrosion in the presence of a film of molten carbonate in air: (a) the general view and (b) the enlarged view of the rectangle in (a).

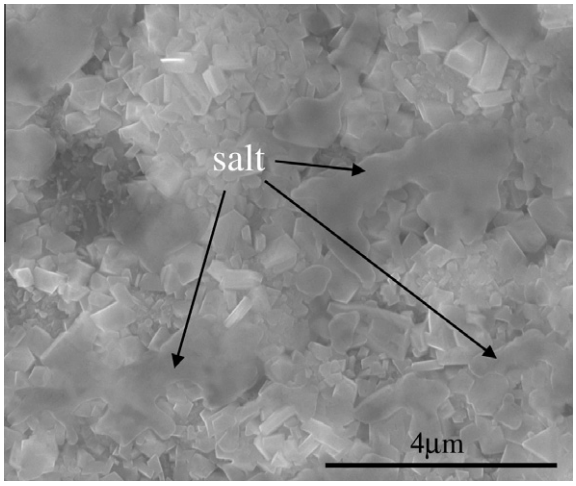

Fig. 11. Surface morphology of 310S of test one after 120 min corrosion in the presence of a film of molten carbonate in air.

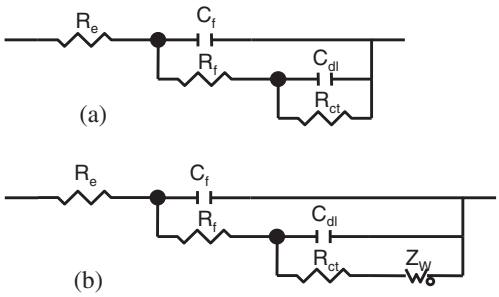

Fig. 12. Equivalent circuits representing the impedance spectra for the corrosion of 310S: (a) equivalent circuit for stage II and (b) equivalent circuit for stage III.

conglomerations of solid salt. However, the fused salt will soak the oxide crystals at 650 °C because of its perfect wettability on the oxides and capillary force.

3.3.3. Interpretation of electrochemical impedance spectra

The alloy forms a porous layer whose interstices are occupied by molten salt at 650 °C. Therefore, the two loops for the corrosion induced by thin molten carbonate represent the impedance responses from the double-layer capacitance at low frequency in parallelism with the oxide capacitance at high frequency, as shown in Fig. 12a. R_e represents the electrolyte resistance, C_{dl} the double-layer capacitance, R_{ct} the charge-transfer resistance, C_f the oxide capacitance, and R_f the oxide resistance. When the diffusion tails come into being in stage III, Warburg resistance Z_w should be added in series with R_{ct}, as is shown in Fig. 12b. Taking into account the dispersion effect, a constant phase angle element (CPE) Q is used to describe the element C_{dl} and C_f in the fitting procedure. The Y_{dl} and n_{dl}, and Y_f and n_f are the constants representing the element Q_{dl} and Q_f, and A_w is the modulus of Z_w which can be represented in the following equation:

$$Z_w = A_w(j\omega)^{-0.5} \tag{5}$$

The simulated values of test one and test two are listed in Table 2 and Table 3, respectively. The values of n_{dl} and n_f deviate greatly from 1, indicating a strong dispersion effect which is common in molten-salt corrosion. Moreover, the values of n_{dl} at the later stage are significantly smaller than those at the initial stage, which may be related with the partial loss of the molten-salt film and the roughness of the surface oxide layer.

In stage II, no Warburg impedance is detected and the value of R_{ct} is several times larger than R_f. However, R_{ct} undergoes rapid decrease in stage II, which can be attributed to the lithiation process that usually occurs after the formation of oxide. An oxide film due to the fast oxidation at stage I partially covered the electrode and blocked the Faradaic current. The newly formed oxides will

Table 2
The parameters of the simulated data for test one.

Time (min)	R_e (Ω cm^2)	Y_f (Ω^{-1} S^{-n} cm^{-2})	n_f	R_f (Ω cm^2)	Y_{dl} (Ω^{-1} S^{-n} cm^{-2})	n_{dl}	R_{ct} (Ω cm^2)	A_w (Ω S$^{0.5}$ cm^2)
20	1.39	2.34×10^{-2}	0.68	1.06	5.24×10^{-2}	0.73	25.04	
26	1.70	1.36×10^{-2}	0.68	1.14	3.18×10^{-2}	0.71	24.15	
32	2.18	1.41×10^{-2}	0.65	1.32	2.70×10^{-2}	0.71	22.30	
38	2.78	1.21×10^{-2}	0.64	1.31	2.66×10^{-2}	0.70	19.12	
48	3.40	6.95×10^{-2}	0.58	1.87	3.95×10^{-2}	0.71	15.85	0.42
56	3.90	2.17×10^{-2}	0.51	1.27	3.84×10^{-2}	0.68	16.02	0.49
62	4.21	1.36×10^{-2}	0.54	1.20	3.88×10^{-2}	0.66	16.73	0.60
69	4.46	1.84×10^{-2}	0.50	1.40	3.94×10^{-2}	0.65	17.28	0.73
75	4.66	1.55×10^{-2}	0.50	1.44	3.95×10^{-2}	0.64	18.40	0.91
82	4.83	1.93×10^{-2}	0.47	1.49	3.93×10^{-2}	0.63	19.64	1.19
88	5.10	1.39×10^{-2}	0.52	1.39	3.93×10^{-2}	0.62	21.66	1.54
94	5.31	1.17×10^{-2}	0.54	1.27	3.92×10^{-2}	0.60	24.51	2.00
101	5.48	1.35×10^{-2}	0.52	1.34	3.89×10^{-2}	0.60	26.86	2.94
107	5.65	6.79×10^{-3}	0.60	1.09	3.95×10^{-2}	0.58	32.31	3.57
114	5.75	1.05×10^{-2}	0.53	1.20	4.03×10^{-2}	0.57	38.17	4.35

Table 3
The parameters of the simulated data for test two.

Time (min)	R_e (Ω cm^2)	Y_f (Ω^{-1} S^{-n} cm^{-2})	n_f	R_f (Ω cm^2)	Y_{dl} (Ω^{-1} S^{-n} cm^{-2})	n_{dl}	R_{ct} (Ω cm^2)	A_w (Ω S$^{0.5}$ cm^2)
25	0.93	2.68×10^{-2}	0.67	0.86	6.84×10^{-2}	0.72	44.52	
40	1.16	1.69×10^{-2}	0.69	1.14	4.11×10^{-2}	0.75	31.80	
55	1.90	1.42×10^{-2}	0.66	1.48	3.06×10^{-2}	0.73	22.20	
70	3.19	2.37×10^{-2}	0.54	2.49	2.12×10^{-2}	0.75	17.73	
85	4.30	2.09×10^{-2}	0.51	1.69	4.08×10^{-2}	0.67	16.55	0.38
100	5.32	1.63×10^{-2}	0.49	2.01	3.89×10^{-2}	0.64	17.38	0.50
115	6.12	1.44×10^{-2}	0.48	2.25	3.77×10^{-2}	0.61	19.71	0.85
130	6.81	1.35×10^{-2}	0.47	2.40	3.70×10^{-2}	0.59	24.53	2.07

immediately precipitate on the alloy surface but their well-known dissolution process in bulk melt [26] was hindered by the limited amount of salt because the concentration of transition metal ions will increase very rapidly to the saturation point in our case. This partial coverage of the oxide film is able to reduce the active area, but the lithiation process is detrimental to the compactness of the oxide film [4]. Even though the initial R_{ct} value of test two is much larger than that of test one, meaning that the blocking effect of the newly formed oxide of test two is more profound, the R_{ct} at the end of stage II was similar owing to a longer stage II or lithiation process.

The value of R_{ct} increases with time after the beginning of stage III, when δ_W is less then 6 mg/cm^2 for both tests. The value of A_w increased rapidly in this stage, suggesting a more difficult diffusion of oxygen ion species in molten salt. Insufficient amount of molten salt in the porous oxide layer would cause twisted diffusion path for the charged ions and the resultant A_w becomes more salient as the molten carbonate continues to loss. The increase of R_{ct} could be also attributed to the severe loss of molten salt, which made the electrochemical process more difficult. However, the A_w is rather small compared with R_{ct} throughout the two runs of experiment. At the end of test, R_{ct}, R_f and A_w value of test two are much smaller than those of test one, indicating a faster corrosion rate of test two as the R_p predicts.

4. Conclusions

EIS has been utilized to monitor the corrosion of 310S induced by thin film of molten carbonate at 650 °C and the monitoring of R_e indicates that the thickness of molten carbonate decreases rapidly to a critical value of 6 mg/cm^2. Larger amount of molten salt on the surface of the electrode causes severer impact of lithiation process. Diffusion process becomes more noticeable at the end of the test due to the limited amount of molten salts.

Acknowledgement

This work was funded by the National Science Foundation of China under the Contract 50971129.

References

[1] B. Zhu, G. Lindbergh, D. Simonsson, Comparison of electrochemical and surface characterization methods for investigation of corrosion of bipolar plate materials in molten carbonate fuel cell: Part II: Surface analysis, Corros. Sci. 41 (1999) 1515–1528.
[2] S. Frangini, Corrosion of metallic stack components in molten carbonate critical issues and recent findings, J. Power Sources 182 (2008) 462–468.
[3] H.S. Hsu, J.H. DeVan, M. Howell, Corrosion of iron in molten carbonates at 650 °C, J. Electrochem. Soc. 134 (1987) 3038–3043.
[4] S. Mitsushima, Y. Nishimura, N. Kamiya, K.I. Ota, Corrosion model for iron in the presence of molten carbonate, J. Electrochem. Soc. 151 (2004) 825–830.
[5] K.N. Lee, D.A. Shores, Transport considerations in the hot corrosion of Ni by molten alkali carbonates, J. Electrochem. Soc. 137 (1990) 859–871.
[6] J.M. Ting, R.Y. Lin, Molten carbonate-induced hot corrosion of nickel, Oxid. Met. 32 (1989) 225–240.
[7] K.I. Ota, K. Toda, S. Mitsushima, N. Kamiya, Accelerated corrosion of stainless steels with the presence of molten carbonate below 923 K, B. Chem. Soc. Jpn. 75 (2002) 877–881.
[8] C.L. Zeng, P.Y. Guo, W.T. Wu, Electrochemical impedance of two-phase Ni–Ti alloys during corrosion in eutectic (0.62Li, 0.38 K)$_2$CO$_3$ at 650 °C, Electrochim. Acta 49 (2004) 2271–2277.
[9] C.L. Zeng, P.Y. Guo, W.T. Wu, Electrochemical impedance spectra for the corrosion of two-phase Cu–15Al alloy in eutectic (Li, K)$_2$CO$_3$ at 650 °C in air, Electrochim. Acta 49 (2004) 1445–1450.
[10] C.L. Zeng, W. Wang, W.T. Wu, Electrochemical-Impedance Study of the Corrosion of Ni and FeAl Intermetallic Alloy in Molten (0.62Li, 0.38 K)$_2$CO$_3$ at 650 °C, Oxid. Met. 53 (2000) 289–302.
[11] B.Y. Yang, K.Y. Kim, The oxidation behavior of Ni–50%Co alloy electrode in molten Li + K carbonate eutectic, Electrochim. Acta 44 (1999) 2227–2234.
[12] F.J. Perez, M.P. Hierro, D. Duday, C. Gomez, M. Romero, L. Daza, Hot-corrosion studies of separator plates of aisi-310 stainless steels in molten-carbonate fuel cells, Oxid. Met. 53 (2000) 375–398.
[13] K. Takeuchi, A. Nishijima, K. UI, N. Koura, C.K. Loong, Corrosion behavior of Fe–Cr alloys in Li$_2$ CO$_3$–K$_2$CO$_3$ molten carbonate, J. Electrochem. Soc. 152 (2005) B364–B368.
[14] S.A. Salih, A.N. El-Masri, A.M. Baraka, Corrosion behavior of some stainless steel alloys in molten alkali carbonate, J. Mater. Sci. 36 (2001) 2547–2555.
[15] S. Frangini, Testing procedure to obtain reliable potentiodynamic polarization curves on type 310s stainless steel in alkali carbonate, Mater. Corros. 57 (2006) 330–337.
[16] B. Zhu, G. Lindbergh, D. Simonsson, Comparison of electrochemical and surface characterisation methods for investigation of corrosion of bipolar plate materials in molten carbonate fuel cell: Part I. Electrochemical study, Corros. Sci. 41 (1999) 1497–1513.
[17] S. Frangini, S. Loreti, The role of temperature on the corrosion and passivation of type 310S stainless steel in eutectic (Li + K) carbonate melt, J. Power Sources 160 (2006) 800–804.
[18] Y.M. Wu, R.A. Rapp, Electrochemical impedance studies of hot corrosion of preoxidized Ni by a thin-fused Na$_2$ SO$_4$ film, J. Electrochem. Soc. 138 (1991) 2683–2690.
[19] G. Gao, F.H. Stott, J.L. Dawson, D.M. Farrell, Electrochemical monitoring of high temperature molten-salt corrosion, Oxid. Met. 33 (1990) 79–94.
[20] D.M. Farrell, F.H. Stott, G. Rocchini, A. Colombo, The influence of electrochemical processes on high-temperature corrosion reactions in combustion system, Mater. High Temp. 10 (1992) 11–19.
[21] C.L. Zeng, J. Li, Electrochemical impedance studies of molten (0.9Na, 0.1K)$_2$SO$_4$-induced hot corrosion of the Ni-based superalloy M38G at 900 °C in air, Electrochim. Acta 50 (2005) 5533–5538.
[22] T.J. Pan, W.M. Lu, Y.J. Ren, W.T. Wu, C.L. Zneg, Electrochemical-Impedance-Spectroscopy (EIS) study of corrosion of steels 12CrMoV and SS304 beneath a molten ZnCl$_2$–KCl film at 400 °C in air, Oxid. Met. 72 (2009) 179–190.
[23] P.L. Spedding, Electrical conductance of molten alkali carbonate binary mixtures, J. Electrochem. Soc. 120 (1973) 1049–1053.
[24] N. Araki, M. Matsuura, A. Makino, T. Hirata, Y. Kato, Measurement of properties of molten salts mixtures of alkaline carbonate salts, Int. J. Thermophys. 9 (1988) 1071–1080.
[25] M. Stern, A.L. Geary, Electrochemical polarization I. a theoretical analysis of the shape of polarization curves, J. Electrochem. Soc. 104 (1957) 56–63.
[26] M. Keijzer, G. Lindbergh, K. Hemmes, P.J.J.M. Van der Put, J. Schoonman, J.H. W de Wit, Corrosion of 304 stainless steel in molten-carbonate fuel cells, J. Electrochem. Soc. 146 (1999) 2508–2516.